

The Prospects of Finding Tidal Disruption Events with 2.5-Metre Wide-Field Survey Telescope (WFST) Based on Mock Observations

Zheyu Lin,^{1,2*} Ning Jiang,^{1,2,3†} and Xu Kong^{1,2,3‡}

¹Department of Astronomy, University of Science and Technology of China, Hefei, 230026, China

²School of Astronomy and Space Sciences, University of Science and Technology of China, Hefei, 230026, China

³Frontiers Science Centre for Planetary Exploration and Emerging Technologies, University of Science and Technology of China, Hefei, Anhui, 230026, China

Accepted 2022 March 31. Received 2022 March 17; in original form 2022 January 11

ABSTRACT

Optical time-domain survey has been the dominant means of hunting for rare tidal disruption events (TDEs) in the past decade and remarkably advanced the TDE study. Particularly, the Zwicky Transient Facility (ZTF) has opened the era of population studies and the upcoming Large Synoptic Survey Telescope (LSST) at the Vera Rubin Observatory (VRO) is believed to further revolutionize the field soon. Here we present the prospects of finding TDEs with another powerful survey to be performed by 2.5-metre Wide-Field Survey Telescope (WFST). The WFST, located in western China, will be the most advanced facility dedicated to optical time-domain surveys in the northern hemisphere once commissioning. We choose to assess its TDE detectability on the basis of mock observations, which is hitherto closest to reality by taking into consideration of site conditions, telescope parameters, survey strategy and transient searching pipeline. Our mock observations on 440 deg² field (CosmoDC2 catalogue) show that 29 ± 6 TDEs can be robustly found per year if observed at u, g, r, i bands with 30-second exposure every 10 days, in which a discovery is defined as ≥ 10 epochal detections in at least two filters. If the WFST survey is fully optimized for discovering TDE, we would expect to identify 392 ± 74 of TDEs every year, with the redshift up to $z \sim 0.8$, which poses a huge challenge to follow-up resources.

Key words: telescopes – transients: tidal disruption events

1 INTRODUCTION

1.1 Tidal Disruption Events (TDEs)

An unlucky star in the core of a galaxy which wanders too close to the supermassive black hole (SMBH) can be torn apart if the tidal force of BH exceeds the self-gravity of the star (Rees 1988; Evans & Kochanek 1989; Phinney 1989). After the disruption, about half of the stellar debris escapes from the BH, while the remaining half is accreted by the BH, producing a luminous flare of electromagnetic emission lasting for months to years. At the peak luminosity, the flare can light up the central region of the galaxy, and even outshine the whole host galaxy. This phenomenon is called as a tidal disruption event (TDE) and has aroused extensive interests because of its unique scientific values. First of all, TDE has provided us an excellent opportunity to investigate the SMBHs in normal galaxies (e.g., Mockler et al. 2019; Pasham et al. 2019), which is otherwise extremely difficult to probe, particularly for dwarf and faraway galaxies. TDEs could even unveil dormant intermediate-mass BHs (IMBHs) (Lin et al. 2018) and SMBH binaries (Liu et al. 2014; Shu et al. 2020). Moreover, TDEs can also serve as an ideal laboratory for exploring the accretion physics of SMBHs, i.e., those unsettled issues in active galactic nuclei (AGNs), by observing the whole life cycle of BH ac-

tivity. Recent progresses in infrared echoes suggest that TDEs have also offered an effective means to study the sub-parsec environments of quiescent SMBHs (e.g. Jiang et al. 2016; van Velzen et al. 2016; Jiang et al. 2021).

However, the observational discoveries of TDEs are quite challenging because of its rather low event rate, which is at orders of $10^{-4} - 10^{-5} \text{ yr}^{-1}$ for most galaxies (e.g., Donley et al. 2002; Gezari et al. 2008; van Velzen & Farrar 2014; van Velzen 2018). Motivated by the theoretical predication of peak spectral energy distributions (SEDs) at soft X-ray or extreme ultraviolet (EUV), TDEs were first identified out as soft X-ray transients in the galactic nuclei with the archival ROSAT data in late 1990s (e.g. Bade et al. 1996; Komossa & Bade 1999). Subsequently, other X-ray instruments, i.e., XMM-Newton, Chandra and Swift, also joined in the journey of discovery one after another (e.g. Esquej et al. 2007; Maksym et al. 2010; Bloom et al. 2011; Saxton et al. 2020), accompanied with a few candidates found in UV bands (e.g. Gezari et al. 2006). Nevertheless, they were all found serendipitously from archival data and thus have scarce synergetic information in other wavelength regimes, which seriously hampered the progress of the field. Until very recently, the SRG/eROSITA all sky survey has shown the power of discovering X-ray TDEs in bulk but with only half-year cadence of light curves (Sazonov et al. 2021).

The number growth of TDEs in the past decade is mainly owing to a variety of wide-field time-domain surveys in optical bands (see recent review of van Velzen et al. 2020; Gezari 2021), such as

* E-mail: linzheyu@mail.ustc.edu.cn

† E-mail: jnac@ustc.edu.cn

‡ E-mail: xkong@ustc.edu.cn

Pan-STARRS (Gezari et al. 2012), PTF (Arcavi et al. 2014), and ASAS-SN (Holoien et al. 2016), even though the origin of optical emission is still under debate (see review of Roth et al. 2020 and recent models of Lu & Bonnerot 2020; Liu et al. 2021). More importantly, these events are noticed in real time, making timely multi-wavelength follow-up observations realistic. Particularly with the commission of the Zwicky Transient Facility (ZTF, Bellm et al. 2019), the cumulative discovery rate of TDEs has increased from $\lesssim 2/\text{yr}$ to $> 10/\text{yr}$, opening the era of statistical research (van Velzen et al. 2021). The dominance of uncovering TDEs in optical bands will be continued, as the Large Survey of Space and Time (LSST) at the Vera Rubin Observatory (VRO) is scheduled to start survey at 2023 (Ivezić et al. 2019). The wide-field and high-cadence survey with 8.4-metre primary mirror telescope ensures VRO to be a milestone for time-domain survey (LSST Science Collaboration et al. 2009). Works from different groups have all predicted that at least thousands of TDEs ($\sim 1,600\text{--}8,000$) per year can be discovered by VRO/LSST (Strubbe & Quataert 2009; van Velzen et al. 2011; Mageshwaran & Mangalam 2015; Thorp et al. 2019; Bricman & Gomboc 2020; Roth et al. 2021).

The unprecedented VRO/LSST will mainly scan the southern celestial sphere while ZTF covers the northern celestial sphere, yet with a much shallower depth. To complement VRO in sky coverage and ZTF in imaging depth, a new time-domain survey is planned with a 2.5-metre Wide-Field Survey Telescope (WFST) in China, which is competitive in discovering various transients. In the following, we will introduce the WFST in details first and then try to estimate its detection rates of TDEs based on mock time-series images.

1.2 Wide-Field Survey Telescope (WFST)

The WFST is being constructed by the University of Science and Technology of China (USTC) and the Purple Mountain Observatory (PMO), and will begin to survey the northern sky at late 2022. This facility is characterized by a 2.5-metre primary mirror and a primary-focus camera with field of view (FOV) of 7 square degrees filled with a 9 pieces of $9\text{K} \times 9\text{K}$ mosaic CCD detector, yielding out an effective FOV of 6.55 square degrees in CCD. The key scientific goals of WFST include: 1) survey the northern sky with the highest sensitivity to explore the variable universe and catch up the time-domain events; 2) find and track one million solar system objects for a panchromatic view of the solar system and understand its kinematic evolution; discover planets or their moons in the Kuiper Belt and beyond; 3) provide high-precision astrometric and photometric catalogues of objects down to $m_r < 25$, allowing precise mapping of the structures of the Milky Way and the nearby universe, which are either science breakthrough such as gravitational events or unknown in the current framework of astrophysics.

During the design study of the WFST, an optical design based on a primary-focus system has been developed. This design features a wide FOV, low obscuration, high efficiency, wide band coverage and high image quality. 80% of the energy of a point source falls within 0.40 arcsec across the full 3-degree field and for all bands. During the design study, special efforts have been paid to increase the system transmission at the u band. This has a great impact on the design choice for the atmospheric dispersion compensator (ADC). To maintain the image quality in real time, an active optics system based on laser tracker measurements and curvature wavefront sensors is proposed. The design of the WFST can be found in Lou et al. (2016), we briefly introduce the optical design, active optics, and the focal-plane instrument in the following passages.

A 3D model of the WFST is shown in Figure 1a. The outlook

of the telescope is dictated by its primary-focus optical layout. The focal-plane instrument and the corrector lenses are mounted as an integrated unit located near the focus of the primary mirror, which is called the primary-focus assembly (PFA). The PFA sits on the top end of the telescope tube via a hexapod, which provide both support and position alignment to the PFA. The primary mirror and mirror cell are located on the other end of the tube. The telescope tube itself is assembled on an altazimuth mount. The top-level telescope specifications are listed in Table 1.

The optical layout of the WFST is shown in Figure 1b. The optical system consists of the primary mirror, 5 corrector lenses, an ADC and six filters. The primary mirror is an $F/2$ aspheric surface with a diameter of 2.5 m. After the corrector lenses, the final system focal ratio becomes $F/2.48$. The primary surface is a hyperbolic concave surface with high-order aspheric terms. The first corrector lens is the largest lens with a diameter of 970 mm. The lens is made of fused silica and has a meniscus shape with a central thickness of 90 mm. The second corrector lens is a negative lens whose concave surface is also a high-order aspheric surface. The third and fourth lenses are all spherical lenses. To control the chromatic aberrations, the third lens is made of Schott's N-BK7 glass. A pair of lensm (lens with a wedge) ADC is inserted between the third and fourth lenses to compensate for the atmospheric dispersion. The fifth lens is a field corrector, which corrects field curvature and reduces distortions. It also serves as the barrier window for the detector dewar.

The WFST PFA is comprised of the mosaic camera, a rolling shutter, filters and filter switch mechanism, and an image rotator. The WFST camera provides a 0.765 Gigapixel flat focal plane array, tiled by 9 pieces of $9\text{K} \times 9\text{K}$ CCD science sensors with $10\ \mu\text{m}$ pixels (CCD290-99 from e2V). This pixel count is a direct consequence of sampling the $6.55\ \text{deg}^2$ FOV ($0.325\ \text{m}$ diameter) with $0.333 \times 0.333\ \text{arcsec}^2$ pixels. Eight additional $4\text{K} \times 4\text{K}$ chips are used for curvature wavefront sensors (surrounded by orange borders in Figure 1c) and four additional chips are used as guiding sensors (shown as green in Figure 1c). The CCD chips, the RAFT structures, and the readout electronics are housed in a vacuum cryogenic dewar, which provides the required working temperature of -100°C for the CCDs (shown as green in Figure 1d). The entrance window to the cryostat is the fifth of the five refractive lenses in the camera. The telescope operates at six wavelength bands (u , g , r , i , z and w), spanning from 320 to 925 nm. An image rotator provides rotation mechanism for the dewar and shutter with respect to the outer frame of the camera. The camera weighs about 460 kg, and its axial position tolerance with respect to the corrector lenses is only $2\ \mu\text{m}$. To reduce the burden on the hexapod that supports the PFA, the camera itself is equipped with a focusing motor, which is able to provide an extra axial adjustment up to $\pm 2\ \text{mm}$.

The site of WFST is on the top of Saishiteng Mountain near the town of Lenghu, Qinghai Province. Its geographical coordinates are $38.6068^\circ\ \text{N}$, $93.8961^\circ\ \text{E}$, and it has an elevation of 4,200 m. The three-year monitoring at a local summit on Saishiteng Mountain has proven it being a world-class astronomical observing site, which have 70% clear nights, median seeing of 0.75 arcseconds and median night sky background of $22.0\ \text{mag/arcsec}^2$ (Deng et al. 2021). Moreover, the Lenghu site in the Eastern Hemisphere, has bridged the huge gap between Mauna Kea, Atacama and the Canary Islands, which will constitute a global network of large observatories ready for great scientific discoveries in the golden time-domain era.

Thanks to its elaborate design and the top-level site condition, WFST is expected to be an excellent hunter for various optical transients, especially the rare ones which can be only captured by advanced time-domain surveys. According to Shi et al. (2018), the

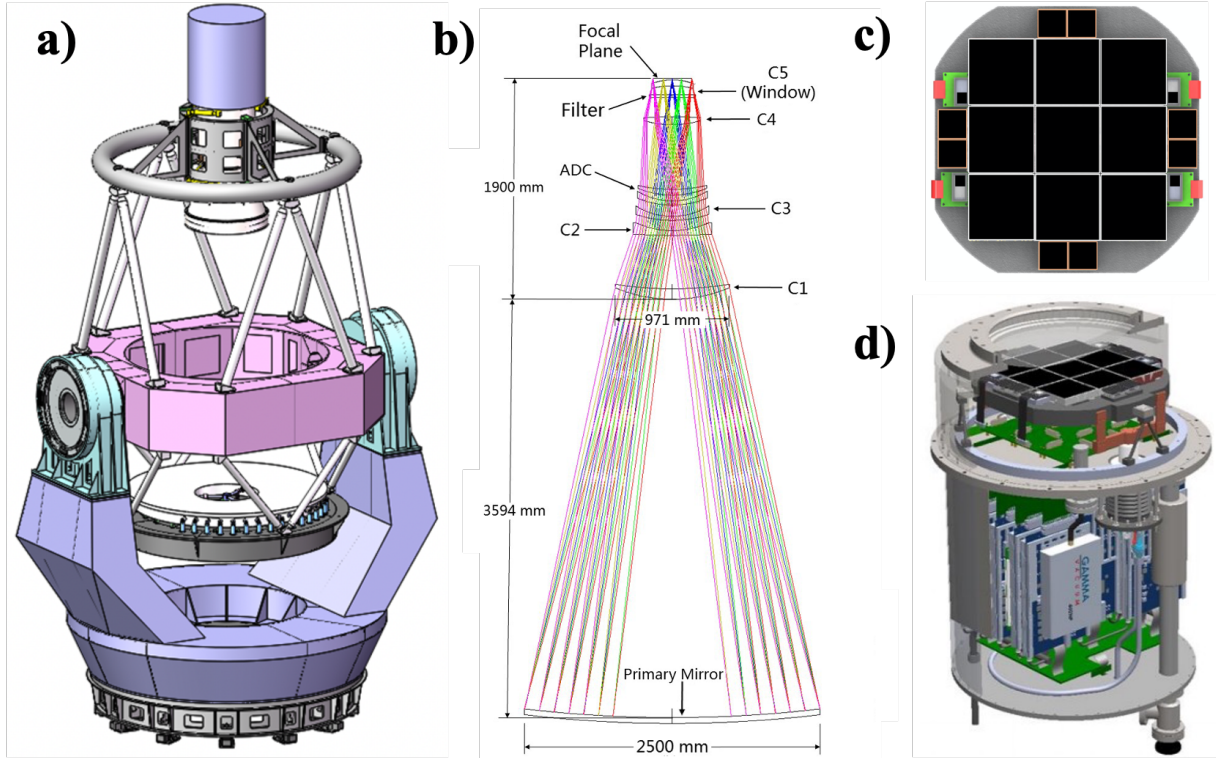


Figure 1. Panel a): 3D model of the WFST; Panel b): Optical layout of the WFST; Panel c): The WFST camera provides a 0.765 Gigapixel flat focal plane array, tiled by 9 pieces of $9K \times 9K$ CCD science sensors with $10 \mu\text{m}$ pixels (white borders). Eight additional $4K \times 4K$ chips are used for curvature wavefront sensors (orange borders), and four additional chips are used as guiding sensors (green); Panel d): A vacuum cryogenic dewar that houses the CCD chips, the RAFT structures, and the readout electronics. It provides the required working temperature of -100°C for the CCDs.

Table 1. Top-level specifications for WFST

Item	Specifications
Optical Configuration	Primary-focus with corrector lenses
Aperture	2.5 m diameter
Focal Length	6.2 m
Field of View	3 deg diameter
Etendue	$29.3 \text{ m}^2 \text{ deg}^2$
Wavelength	320-925 nm (<i>u</i> , <i>g</i> , <i>r</i> , <i>i</i> , <i>z</i> , <i>w</i>)
Image Quality	Diameter ≤ 0.4 arcsec (80% energy encircled)
Plate Scale	30 mm/arcsec
Pixel Size	$10 \mu\text{m} \times 10 \mu\text{m}$
Number of pixels	0.765 Giga
Survey Depth	$m_u = 22.31$, $m_g = 22.93$, $m_r = 22.77$, $m_i = 22.05$, $m_z = 21.02$, $m_w = 22.96$ for 30s exposures

$5\text{-}\sigma$ limiting magnitude for a 30-second exposure in each band is: $m_u = 22.31$, $m_g = 22.93$, $m_r = 22.77$, $m_i = 22.05$, $m_z = 21.02$, $m_w = 22.96$.

In this work, we choose to focus on the detectability of TDEs quantitatively with mock observations by taking into account of dif-

ferent factors. The methods and procedure involved are introduced in Section 2 and 3. Then we will show the main results from mock observations in Section 4 and end with a brief conclusion in Section 5.

2 METHOD

In this section, we introduce the parameterized models used to generate light curves and host galaxies of TDEs.

2.1 Galaxy Catalogue

The demand of host galaxy information for mock observation is three-folds. First, in reality, a TDE candidate is identified only when it is associated with the centre of a galaxy. Second, the emission of tidal disruption flare (TDF) will be unavoidably diluted by its host galaxy, in the form of background contamination and dust extinction. Third, the host galaxy could provide additional parameters required by the MOSFiT TDE model (see Section 2.3).

We finally choose CosmoDC2, a synthetic galaxy catalogue that contains ~ 2.26 billion galaxies in a sky area of 440 deg^2 (Korytov et al. 2019). The galaxies in this field match with the expected number densities from contemporary VRO/LSST surveys to $m_r = 28$ and $z = 3$. Each galaxy comprises an exponential disk component and a bulge component with Sérsic index $n = 4$. In addition, the redshift z and central black hole mass M_{BH} are both given for each galaxy, and the rest-frame spectral energy distributions (SEDs) from 100 to 2,000 nm for each component are also provided, enabling the calculation for fluxes and AB magnitudes in WFST bands. Moreover, the morphological parameters needed to reconstruct the disk and bulge images (e.g., half-light radius R_e , ellipticity) are all included by the catalogue.

The galaxy number of the whole catalogue is however tremendous. We have first abandoned those which are obviously beyond the parameter spaces considered in this work. The detailed steps are presented as below.

(i) Exclude galaxies at $z > 1.5$, as TDEs at such high redshift are too faint to be observed. This cut will get rid of a large fraction of galaxies since most galaxies in the catalogue are located at $1.5 < z < 3$ actually.

(ii) Exclude galaxies with $M_{\text{BH}} < 10^5 M_{\odot}$. Theoretically, TDEs can occur in these galaxies, e.g., tidal disruption of white dwarfs by intermediate-mass black holes (see review by Maguire et al. 2020). However, their physical details, and thus their anticipated optical light curves remain rather unclear.

(iii) Exclude galaxies with $M_{\text{BH}} > M_{\text{Hills}}$. The Hills mass M_{Hills} is the maximum mass for a Schwarzschild BH, whose event horizon keeps inside of the tidal radius. It is defined as

$$M_{\text{Hills}} = 9.0 \times 10^7 M_{\odot} \left(\frac{M_{\star}}{M_{\odot}} \right)^{-1/2} \left(\frac{R_{\star}}{R_{\odot}} \right)^{3/2} \quad (1)$$

(Hills 1975; Beloborodov et al. 1992; Leloudas et al. 2016). We have applied a Kroupa IMF, whose minimum and maximum stellar masses are $0.08 M_{\odot}$ and $1 M_{\odot}$, respectively, and used the relation $R_{\star} \propto M_{\star}^{0.8}$ on lower main sequence (Stone & Metzger 2016) to get $M_{\text{Hills}} \propto M_{\star}^{0.7}$. As a result, galaxies with $M_{\text{BH}} \geq 9.0 \times 10^7 M_{\odot}$ have been excluded since M_{BH} exceeds the maximum Hills mass in this mass range.

The three criteria above have readily rejected most galaxies, with the remaining number decreases down to about 52 million.

2.2 Selecting Galaxies hosting TDEs

The galaxy number after the primary cut above is still very large and will be extremely time-consuming if we model all of them. In fact, the TDE rate for a given galaxy is very low, meaning that TDEs

will occur only in a very small fraction of these galaxies within one year. Therefore, we choose to first pick out the galaxies with real TDE occurrence in the mock observations and neglect others. The adopted TDE rate is the one given by Stone & Metzger (2016) with the modification of cosmological effect, that is

$$\begin{aligned} \dot{N}_{\text{TDE}}(z) &= \dot{N}_{\text{TDE},0} \frac{dt_0}{dt} \\ &= 10^{-4.19} \frac{1}{1+z} \left(\frac{M_{\text{BH}}}{10^8 M_{\odot}} \right)^{-0.223} \text{yr}^{-1}, \quad (2) \end{aligned}$$

where t_0 and t are the time in the frame of the source and the observer, respectively.

With knowing of the TDE occurrence rate of a specific galaxy assigned by Equation 2, we then determine whether or not there happens a TDE within one year. Only if the galaxy has been picked out as a TDE host in the simulation, we take it for further consideration. For simplicity, we assume one galaxy can undergo at most one TDE per year.

We have performed the selection process for 100 times in order to minimize the random errors induced in the selection process. The averaged number obtained is $5,192 \pm 62$, that is an event rate of $\sim 0.01\%$ for these galaxies. The reduced number up to this step becomes basically acceptable.

2.3 TDF light curves generated by MOSFiT

The classical theory has predicted a $t^{-5/3}$ decline in the light curves of the tidal disruption flare (TDF), which is purely determined by the mass fall-back rate of stellar debris after disruption. Observationally, optical surveys have yielded out dozens of TDEs with well-sampled light curves so far (van Velzen et al. 2020; Gezari 2021). They show somewhat consistency but also discrepancy with the theoretical prediction. Therefore, it is improper to create optical light curves crudely from theory and some empirical models have been developed to fit the observational data better. The MOSFiT, one of such kind of models, is exactly designed to help bridge the gap between observations and theories for different types of transients (Guillochon et al. 2018). In addition to fitting the light curves of known TDEs, MOSFiT also yields statistically consistent predictions for other characteristics, for instance, the M_{BH} (Mockler et al. 2019), proving that it is a reliable model.

Specifically, 11 parameters have been used to generate light curves by MOSFiT. We introduce these parameters and their settings as follows:

- (i) Redshift z .
- (ii) Black hole mass M_{BH} .

For z and M_{BH} , we apply the values directly from the galaxy catalogue we use.

(iii) Hydrogen column density N_{H} . MOSFiT uses a ratio $N_{\text{H}} = 1.8 \times 10^{21} A_{\text{V}}$ to convert A_{V} into N_{H} . To calculate A_{V} at the galaxy centres, we refer to the calculation method of Roth et al. (2021). First, we obtain $A_{\text{H}\alpha}$ for each galaxy. Galaxies that have specific star-formation rate $\text{sSFR} > 10^{-11.3} \text{ yr}^{-1}$ are classified as star-forming galaxies, while the rest are labelled as quiescent galaxies. For star-forming galaxies, $A_{\text{H}\alpha}$ is drawn from a Gaussian distribution with a floor at zero, where the median is described by an equation that only related to the stellar mass of the

host galaxy,

$$A_{H\alpha, \text{median}} = 0.91 + 0.77x + 0.11x^2 - 0.09x^3, \text{ where} \quad (3)$$

$$x \equiv \log_{10} \left(\frac{\text{host } M_{\star}}{10^{10} M_{\odot}} \right),$$

and the standard deviation is 0.28 mag. This relationship was only calibrated for star-forming galaxies with total stellar mass between $10^{8.5}$ and $10^{11.5} M_{\odot}$ by Garn & Best (2010), therefore we use the edge values of the equation for star-forming galaxies with $M_{\star} < 10^{8.5} M_{\odot}$ and $M_{\star} > 10^{11.5} M_{\odot}$. For quiescent galaxies, we draw A_V from a Gaussian distribution whose median and standard deviation are 0.2 and 0.06 mags, respectively, with a floor at zero. This choice of median is based on the results of González Delgado et al. (2015). We then adopt the Calzetti et al. (2000) law and $R_V = 4.2$ to convert all $A_{H\alpha}$ into A_V . Finally, the host galaxy and the Galactic dust extinctions are applied to each event according to the model in O'Donnell (1994).

We realize that CosmoDC2 has provided dust extinction parameters A_V and R_V . However, both parameters are found too low to describe TDEs that take place in galaxy centres. Therefore, we choose the method of Roth et al. (2021) to estimate the dust extinction.

(iv) The reprocessing layer can help explain the optical/UV emission of TDFs. In this model, it is assumed as a simple blackbody photosphere, and its radius has a power-law dependence on luminosity, defined as

$$R_{\text{phot}} = R_{\text{ph0}} a_p (L/L_{\text{Edd}})^l, \quad (4)$$

where a_p is the semimajor axis of the accreting mass at peak \dot{M}_{fb} , and $L_{\text{Edd}} \equiv 4\pi GM_{\text{BH}}c/\kappa$ is the Eddington luminosity. This equation contains two free parameters: the power-law exponent l and radius normalization R_{ph0} .

(v) Variance parameter σ .

(vi) Explosion time t_{exp} , when the TDE starts.

(vii) Viscous time T_{viscous} , defined as

$$\dot{M}_{\text{d}}(t) = \dot{M}_{\text{fb}}(t) - \dot{M}_{\text{d}}(t)/T_{\text{viscous}}, \quad (5)$$

where \dot{M}_{d} is the mass that remains suspended outside of the black hole's horizon for roughly a viscous time, and \dot{M}_{d} is the accretion rate onto the black hole from the forming disk.

For l , R_{ph0} , σ and T_{viscous} , we refer to the fitting results from the 14 TDEs in Mockler et al. (2019), and set $l = 1.5$, $\log_{10}(R_{\text{ph0}}) = 0.8$, $\sigma = 0.1$, $T_{\text{viscous}} = 0.001 - 0.5$. We have noticed that the light curve production needs at least one free parameter and T_{viscous} has been chosen by us. Actually, the light curves with different T_{viscous} values show extremely weak discrepancy in our experiments. Also, it should be emphasized that though the settings of $l = 1.5$, $\log_{10}(R_{\text{ph0}}) = 0.8$ are the default settings of the MOSFiT TDE model, and representative for known TDEs (Mockler et al. 2019), a broader range of values is possible and might affect our results as the light curve modelling is sensitive to l and R_{ph0} . However, it is beyond the scope of this work.

(viii) Radiative efficiency ϵ .

We set $\epsilon = 0.1$. We note that the efficiency ϵ varies from 0.006 to 0.2 in the real fitting (Mockler et al. 2019). However, we still simply adopt the most conventional value 0.1 given our poor knowledge of the distribution of ϵ in different TDEs.

(ix) Stellar mass M_{\star} .

As introduced above, we adopt a Kroupa IMF, whose minimum and maximum stellar masses are $0.08 M_{\odot}$ and $1 M_{\odot}$, respectively.

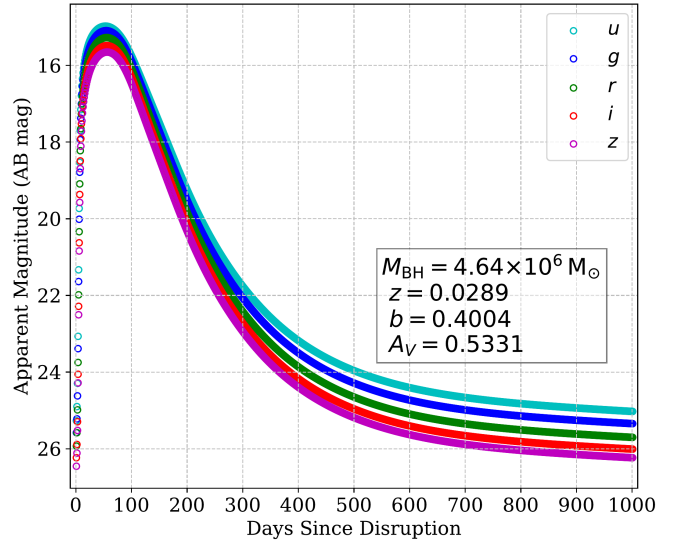


Figure 2. An example of TDF light curves at WFST u , g , r , i and z bands generated by MOSFiT model. The light curves have been sampled from day 1 to 1001 since disruption with an interval of one day.

(x) Scaled impact parameter b . It is a proxy for the impact parameter β .

For b , we referred to the assumption of Bricman & Gomboc (2020), that the probability for an encounter with a pericentre distance between R_p and $R_p + dR_p$ is proportional to the area $2\pi R_p dR_p$, and the corresponding distribution function of β :

$$p(\beta) = \frac{1}{2\beta^3} \left(\frac{1}{\beta_{\text{min}}^2} - \frac{1}{\beta_{\text{max}}^2} \right)^{-1}. \quad (6)$$

where

$$\beta_{\text{min}} = \beta(b=0), \quad \beta_{\text{max}} = \min[\beta(R_p = 2R_S)],$$

$$\beta(R_p = 2R_S) = 11.8 (M_{\text{BH}}/10^6 M_{\odot})^{-2/3} (M_{\star}/M_{\odot})^{7/15}. \quad (7)$$

The selection of $\beta(b=0)$ and β will be explained below. Then we convert β into b . According to the work of Guillochon & Ramirez-Ruiz (2013) based on the polytropic models, for a star with $\gamma = 4/3$, minimum disruptions correspond to $b = 0$ and $\beta = 0.6$, full disruptions correspond to $b = 1$ and $\beta = 1.85$, and disruptions with $b = 2$ correspond to $\beta = 4.0$. While for a star with $\gamma = 5/3$, $b = 0, 1, 2$ correspond to $\beta = 0.5, 0.9, 2.5$, respectively. The MOSFiT TDE model uses a hybrid polytropic model that blends between $\gamma = 4/3$ and $\gamma = 5/3$, in which a fraction of $\gamma = 5/3$ is defined as

$$f = \begin{cases} 1, & (0.08 \leq M_{\star}/M_{\odot} \leq 0.3) \\ 1 - \frac{(M_{\star}/M_{\odot}) - 0.3}{1.0 - 0.3}, & (0.3 < M_{\star}/M_{\odot} \leq 1.0) \end{cases} \quad (8)$$

within the mass range from which we drew (Mockler et al. 2019). Therefore, for a star with $0.08 \leq M_{\star}/M_{\odot} \leq 1.0$, its

$$\begin{aligned} \beta(b=0) &= 0.5f + 0.6(1-f) = 0.6 - 0.1f = \beta_{\text{min}}, \\ \beta(b=1) &= 0.9f + 1.8(1-f) = 1.8 - 0.9f, \\ \beta(b=2) &= 2.5f + 4.0(1-f) = 2.5 - 1.5f. \end{aligned} \quad (9)$$

Using a piecewise linear function $b = b(\beta)$, and setting an upper limit of $b_{\text{max}} = 2$, we finally finish the conversion from β to b .

After setting these parameters, and convolving with the WFST filter throughput curves, the generated light curves of a TDE at u , g , r , i , z bands are obtained (see an example in Figure 2). For

each galaxy, we have drawn 10 pairs of M_\star and b , and then drawn 10 A_V for each pair, and correspondingly, generated 100 light curves.

We have implemented a final selection before the mock observation. If the peak magnitudes of a TDE (TDF plus host) are below the WFST 30-second limiting magnitudes, that are $m_u = 22.31$, $m_g = 22.93$, $m_r = 22.77$, $m_i = 22.05$, $m_z = 21.02$ (Shi et al. 2018), we exclude the source out as it is beyond the detection threshold. This will get rid of $\sim 90\%$ galaxies.

3 MOCK OBSERVATION AND DETECTION

After host galaxies and TDF light curves prepared, we introduce mock observations and detection criteria in this section. We assume a simple uniform survey strategy for the experimental 440 deg^2 CosmoDC2 field, which will be scanned with 30-second single exposures every 10 days at u, g, r, i, z band, respectively. In reality, a specific source can be only well observed during half-time in a year, thus we put "observation windows" spanning 180 days in the timeline. On the other hand, the clear night proportion, that is about 70% defined as more than 4 hours of contiguous fully clear time (Deng et al. 2021), has been also considered.

3.1 Mock images

We begin with generating mock images of host galaxies using the open-source simulation tool GalSim (Rowe et al. 2015). First, the pixel size is fixed to the one used by WFST CCD, that is $0.333''/\text{pixel}$. The galaxy surface brightness distribution at a given band, comprising an exponential disk and a Sérsic bulge, is derived from its morphological parameters and SED. TDF appears as a point source in the galaxy centre. However, the real images are much more complicated as they will be blurred by atmospheric seeing and contaminated by noises.

3.1.1 Seeing

The atmospheric seeing of Lenghu Site is being monitored and publicly available¹. We blurred images at different epochs with Gaussian point spread functions (PSFs), whose full width at half maximum (FWHM) is equal to the seeing values at that epoch. The assigned seeing at different epochs obeys the probability distribution from monitoring (median $0.78''$).

3.1.2 Noise

We consider two origins of noises. One is the Poisson noise and the other is the readout noise. First, the Poisson noise obeys the Poisson distribution,

$$P(k, N) = \frac{N^k}{k!} e^{-N}, \quad k \in \mathbb{N}_0, \quad (10)$$

where N is the total count from astronomical sources and sky background in each pixel. The readout noise is subject to a standard normal distribution: $X \sim \mathcal{N}(\mu, \sigma^2)$, where $\mu = 0$, and σ is set to $10 e^-/\text{pixel}$.

¹ <http://lenghu.china-vo.org/sitecondition>

3.2 Reference Images

In addition to mock images for a single visit, we further need to construct reference images since almost all modern time-domain surveys have chosen to detect transients in the reference-subtracted difference images directly or by comparing with the photometry on reference images. The reference images are normally created by stacking high quality images to a depth deeper than individual images. Here we simply define the images observed under conditions of seeing $\leq 0.7''$ as being good enough to be stacked. If the first-year survey has uniformly scanned the whole northern sky at all five bands, we can obtain reference images identical to a seeing of $0.7''$ and an exposure time of 100 seconds in each band.

3.3 Light curves from PSF photometry

The PSF photometry has been widely applied for transient detection by time-domain surveys nowadays, either in difference images or original images, because it can effectively reduce the impact from starlight for detecting transients embedded in galaxies, such as TDEs in galaxy centres. The specific PSF photometry code we used is PythonPhot (Jones et al. 2015) which has also considered the noise images well. For each observation (in a given filter on a certain day), the PSF image is produced by `getpsf` function assuming its FWHM is approximately identical with seeing.

We take the difference of PSF photometry between a single-visit and reference image as the contribution from TDF. Before this step, we have convolved the images with better seeing with Gaussian function to ensure they share the same imaging quality. The PSF photometry is principally self-consistent and precise only for point sources. Nevertheless, the TDF emission overlapped with its extended host galaxy is certainly not a strict point source. To check the systematic errors, we have compared the derived TDF emission from our strategy with the one predicted from MOSFiT model. It suggests that they agree with each other at most epochs, albeit with large errors at late stages when TDF emission becomes very weak and thus being overwhelmed by starlight (see Figure 4). Generally, the measurement from the difference of PSF photometry is acceptable for our simulation.

3.4 Criteria for TDE detection

After acquiring the TDE light curves by our measurements (as shown in Figure 4), we can then check and define the detection criteria for a TDE. We use two key parameters, that is the difference as measured from PSF photometry ($\Delta N = N_{\text{gal+TDF},30s} - N_{\text{gal},30s}$) and their errors ($\sigma_N = \sqrt{(\Delta N_{\text{gal+TDF},30s})^2 + (\Delta N_{\text{gal},30s})^2}$).

A host galaxy detected in a band of WFST should satisfy this condition

$$\frac{N_{\text{gal},100s} - N_{\text{lim},100s}}{\Delta N_{\text{gal},100s}} > s_1, \quad (11)$$

where the limiting count $N_{\text{lim},100s}$ stands for the counts of a 100-second exposure to a source having an apparent magnitude that equals to the $5\text{-}\sigma$ limiting magnitude, $m_{\text{lim},100s} \approx m_{\text{lim},30s} + 1.25 \log_{10}(10/3)$, and a TDE detected in a band of WFST should satisfy these two conditions

$$m_{\text{gal+TDF}} < m_{\text{lim},30s} - \Delta m; \quad (12)$$

$$\frac{\Delta N}{\sigma_N} > s_2 \quad (13)$$

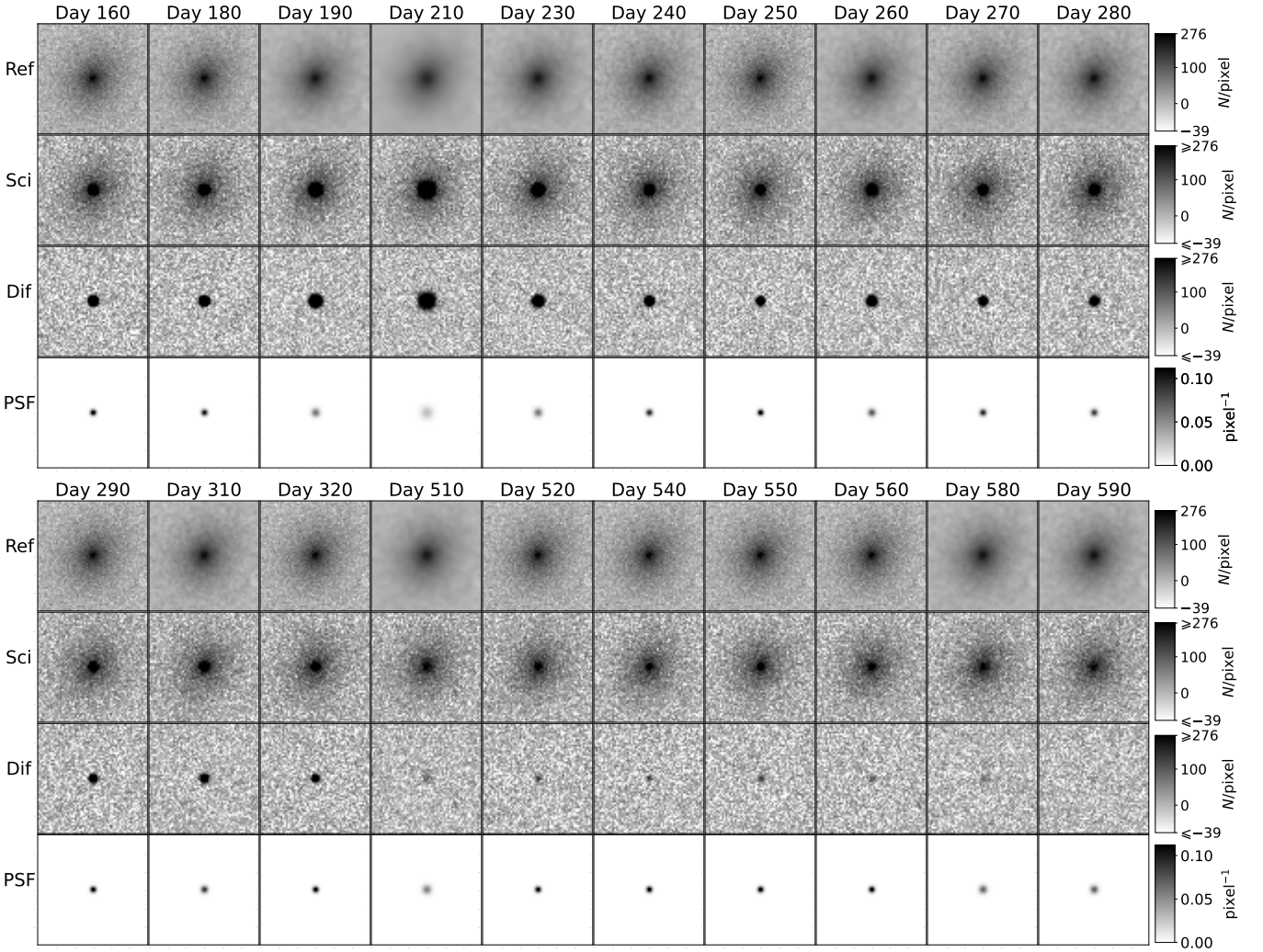


Figure 3. The reference, science, difference and PSF images (from top to bottom) at different stages for a typical detectable TDE at $z = 0.0452$. "Observation windows" have been put onto the timeline. Each "window" lasts for 180 days, and the intervals are also set as 180 days. Besides, a clear night proportion for WFST, about 70%, is also considered, making the final timeline. The seeing of original reference images is $0.7''$. The reference images are convoluted to match the atmospheric seeing of the science images if the seeing is worse than $0.7''$ (e.g., Day 210), and vice versa (e.g., Day 250). We note that the difference images are still far from reality, therefore we performed photometry only on reference and science images.

for k times.

For u , g , r , i and z band, a detectable TDE should be detected in at least l_1 band(s), with its host galaxy detected in at least l_2 band(s). We set $s_1 = s_2 = 3$, $\Delta m = 1$, $k = 10$, $l_1 = 2$, $l_2 = 1$. As mentioned above, $m_{\text{lim},30\text{s}}$ of five WFST bands are $m_u = 22.31$, $m_g = 22.93$, $m_r = 22.77$, $m_i = 22.05$, $m_z = 21.02$.

4 RESULTS

In this section, we will present the results from our mock observations and try to analyse the impact by different factors, e.g., band selection, noise and sampling cadence.

4.1 Noise & Band combination

Lenghu Site has sky background monitoring data in the Sky Quality Metre (SQM) photometric system (Cinzano 2005). However, the conversion factors from SQM readings to WFST bands are quite uncertain, so we just simply estimate the influence by setting several

typical sky background values. We have tested six levels of sky backgrounds, that are $I_{\text{sky}} = 17, 18, 19, 20, 21, 22 \text{ mag/arcsec}^2$. Likewise, the readout noise has been also taken into account. The impact of noise to the signal detection can be easily seen in Figure 5.

We have also checked the affection of noise to observations with different band selections, which is presented in Table 2. We may immediately conclude from them as below.

- (i) The sky background affects the results significantly when $I_{\text{sky}} < 20 \text{ mag/arcsec}^2$.
- (ii) The readout noise slightly influences the whole detection rate with an exposure time of 30 seconds for single visit. It not only contaminates the TDF emission, but also impedes the detection of host galaxies, especially at high redshifts.
- (iii) g and r are the most crucial bands for TDE detection.
- (iv) u band cannot significantly increase the detection rate directly once both g and r bands have been adopted. The uselessness for detection is mainly due to the shallow magnitude limit in u band. The difference between the limiting magnitude of u and r band is $u_{\text{lim}} - r_{\text{lim}} = -0.46$, which is smaller than that of galaxies and most

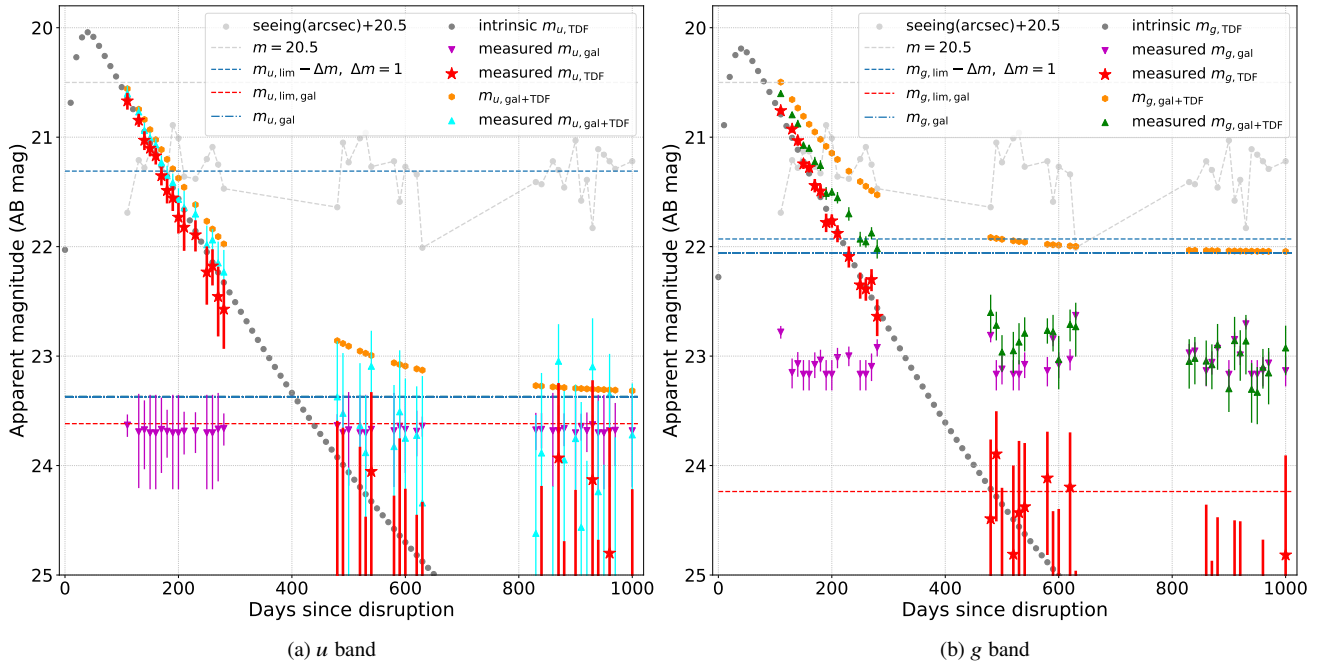


Figure 4. The light curves of a TDE at $z = 0.253$ as an example of our mock observations. The left and right panel show u and g band results, respectively. The measured TDF light curves with 1σ errors are shown in red, which is calculated as the difference between the PSF photometry on the reference image and single-epoch observed image. For the ease of comparison, we have also plotted the intrinsic galaxy magnitude (blue dashed lines), intrinsic TDF magnitude given by MOSFiT (dark grey dots), 30-second (for science images, blue dashed) and 100-second (for reference images, red dashed) limiting magnitude in the corresponding band. The seeing value at each epoch is also shown in light grey.

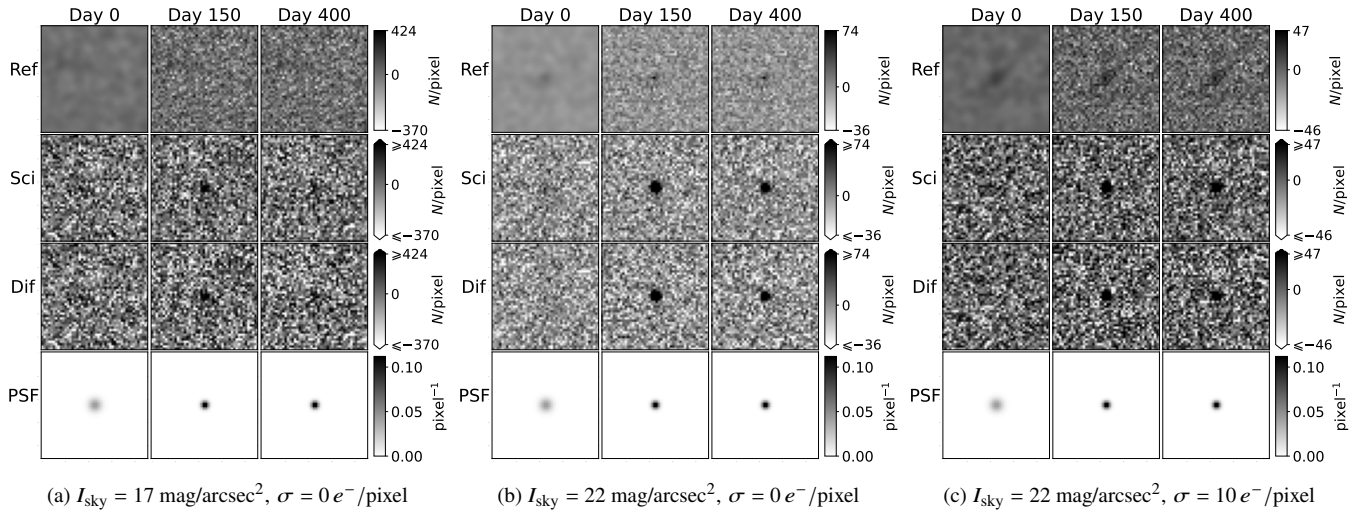


Figure 5. Illustrations for the impact of sky background and readout noise. Panel (a) shows the reference, science, difference and PSF images (from top to bottom) for a TDE observed with $I_{\text{sky}} = 17 \text{ mag/arcsec}^2$, $\sigma = 0 e^-/\text{pixel}$, i.e., no readout noise. (b): $I_{\text{sky}} = 22 \text{ mag/arcsec}^2$, $\sigma = 0 e^-/\text{pixel}$. (c): $I_{\text{sky}} = 22 \text{ mag/arcsec}^2$, $\sigma = 10 e^-/\text{pixel}$.

TDFs, as shown in top panels of Figure 6. However, u band should play a key role in the SED fitting of TDEs as most optical-UV TDEs have the blackbody temperature T_{bb} in the range of 10,000 to 50,000 Kelvin (van Velzen et al. 2020), corresponding to the rest-frame peak wavelength range of 580 to 2900 Å. Therefore, the u -band, which is closest to the SED peak among all filters, would be very useful to constrain the SED in the practical transient classification. For this reason, we will still recommend a selection of u band in the TDE search.

- (v) z band cannot significantly improve the detection rate of TDEs,

since the difference between the limiting magnitude of i and z band is $i_{\text{lim}} - z_{\text{lim}} = 1.03$, which is larger than the $i - z$ of TDFs and host galaxies (see bottom panels of Figure 6). Moreover, it can hardly put effective constraints on the SED fitting, that is distinct from u band. Therefore, we will abandon z band in the considerations of filters.

4.2 Threshold & Cadence

Mock observations were then performed on the first 10 groups of galaxies, with 100 observations per group. In default, we set threshold

Table 2. Results of $10 \times 10 \times 10$ mock observations: The impact of sky background and readout noise

I_{sky} (mag/arcsec ²)	17	18	19	20	21	22	22	
Readout noise (e^-/pixel)	10	10	10	10	10	10	0	
Used Bands	<i>ug</i>	3(74)	5(128)	7(187)	9(237)	10(264)	11(290)	11(299)
	<i>ur</i>	5(124)	8(226)	12(327)	15(408)	17(449)	17(460)	18(481)
	<i>ui</i>	3(92)	6(172)	10(262)	12(330)	13(359)	14(373)	15(389)
	<i>gr</i>	5(146)	10(275)	16(437)	23(610)	27(712)	28(757)	30(804)
	<i>gi</i>	4(99)	7(187)	11(292)	14(378)	16(419)	17(445)	17(467)
	<i>ri</i>	4(107)	8(207)	12(317)	15(408)	17(446)	17(466)	18(487)
	<i>ugr</i>	6(106)	11(193)	17(301)	23(415)	27(482)	29(512)	30(543)
	<i>ugi</i>	5(98)	9(166)	13(239)	16(290)	18(322)	19(339)	20(359)
	<i>uri</i>	5(97)	10(173)	14(252)	17(312)	19(344)	20(358)	21(378)
	<i>gri</i>	6(113)	12(208)	18(315)	24(428)	27(488)	29(515)	31(548)
	<i>ugri</i>	7(91)	12(163)	18(244)	24(327)	28(372)	29(392)	31(417)
	<i>ugriz</i>	7(74)	12(130)	18(195)	24(261)	28(297)	29(314)	31(333)

Notes:

1. Out of parentheses: Detectable TDEs in 440 deg^2 per year, with sky background level, readout noise and band combination altered.

2. In parentheses: Detectable TDEs in maximum survey area per year, with sky background level, readout noise and band combination altered. The maximum survey area are calculated based on the WFST scanning speed (assuming 4-hour useful observing time per night, 10-second readout time), with an upper limit of 2π steradian ($\sim 20,600 \text{ deg}^2$) if the band combination can fully cover the full northern celestial sphere.

$k = 10$, cadence $C = 10$ d, as introduced in Section 3.4. Changing either of them might significantly affect the results, hence we set $k = 5$ and $C = 20$ d. We have kept $s_1 = s_2 = 3$, $\Delta m = 1$, $l_1 = 2$, and $I_{\text{sky}} = 22 \text{ mag/arcsec}^2$. The results are shown in Table 3. WFST can cover the full northern celestial sphere within a ~ 35 -hour observing period in a single filter. Consider an average exposure of 4 hours per night, we note that even $C = 20$ d cannot cover the full northern celestial sphere in more than two filters.

Table 3 indicates that higher cadence and lower threshold will result in higher detection rates, in agreement with our expectation.

4.3 Host galaxy detection

The host galaxy detection is crucial for the identification of TDE candidates from numerous of unclassified transients because the isolated or off-nuclear transients, which are vast majority, can be cast away with the aid of the association with host galaxy. Deeper reference images or those taken from other value-added catalogues could greatly benefit the host detection. For the former one, the results based on 100-second (i.e., one-year survey on the northern sky) reference images have been shown above, while the latter is beyond the scope of our work.

Additionally, the characteristics of host galaxies (e.g., colour) might also provide useful clues to transient classification before any follow-up observations. For this reason, the host galaxy is better to be detected in more than two bands, i.e., $l_2 = 2$. We have checked its affection and displayed main results in Table 3, with $s_1 = s_2 = 3$, $\Delta m = 1$, $l_1 = 2$ retained. More details are shown in appendix (see Table A1).

4.4 Comparison with real optical TDE sample

In this section, we will show the distribution of TDEs detected in our mock observations, and compare them with the 33 optical TDEs summarized in van Velzen et al. (2020). Parameters set in these mock observations are: $s_1 = s_2 = 3$, $\Delta m = 1$, $k = 10$, $l_1 = 2$, $l_2 = 1$, $C = 10$ d, *ugri* bands.

4.4.1 Redshift and M_{BH} distribution

The redshift distribution of TDEs detected in our mock observations is shown in Figure 7. The higher-redshift TDEs call for deeper imaging, not only for the detection of the TDF emission itself, but also for the host galaxies, which is essential for identifying TDE candidates in the real observations. If the host galaxy detection is performed along with the 100-second exposure image, the redshift of TDEs can be up to $z \sim 0.8$ (median ≈ 0.23), that is already higher than the most distant optical TDE, AT2020riz at $z = 0.435$, found to date.

We show the joint distribution of z and M_{BH} in Figure 8. The detected TDEs are mainly distributed in the region of $z \sim 0.2 - 0.3$ and $M_{\text{BH}} \sim 10^6 - 10^7 M_{\odot}$, that is roughly consistent with the prediction of VRO/LSST observations (Roth et al. 2021, their Figure 24). Obviously, M_{BH} tends to be lower at lower redshifts. It can be readily understood as a natural result of BH-host galaxy correlation since low-mass BHs usually reside in dwarf galaxies. More fainter galaxies are more easily detected in lower redshifts.

4.4.2 M_g distribution

In Figure 9 we show the distribution of absolute g -band magnitude (M_g) as a function of redshift. The flux limit determines that only brighter TDEs can be detected at higher redshift. Our TDE sample has kept its maximum luminosity around that of the brightest optical TDE, ATLAS18yzs, indicating reasonable parameter settings. Besides, it has extended to higher redshift than known optical TDEs.

The sparser distribution of our sample at $z < 0.1$ is probably due to the small number of galaxies at such low redshift. Actually, galaxies at $z < 0.1$ only occupy $\sim 0.07\%$ among the total 52 million ones, leading to the very few TDEs found in a small sky region (440 deg^2).

4.4.3 Luminosity function

To further examine the reliability of the results, we have calculated the luminosity function (LF) of the detected TDEs at $z < 0.4$ using the " $1/V_{\text{max}}$ " method introduced in van Velzen (2018), and find it is

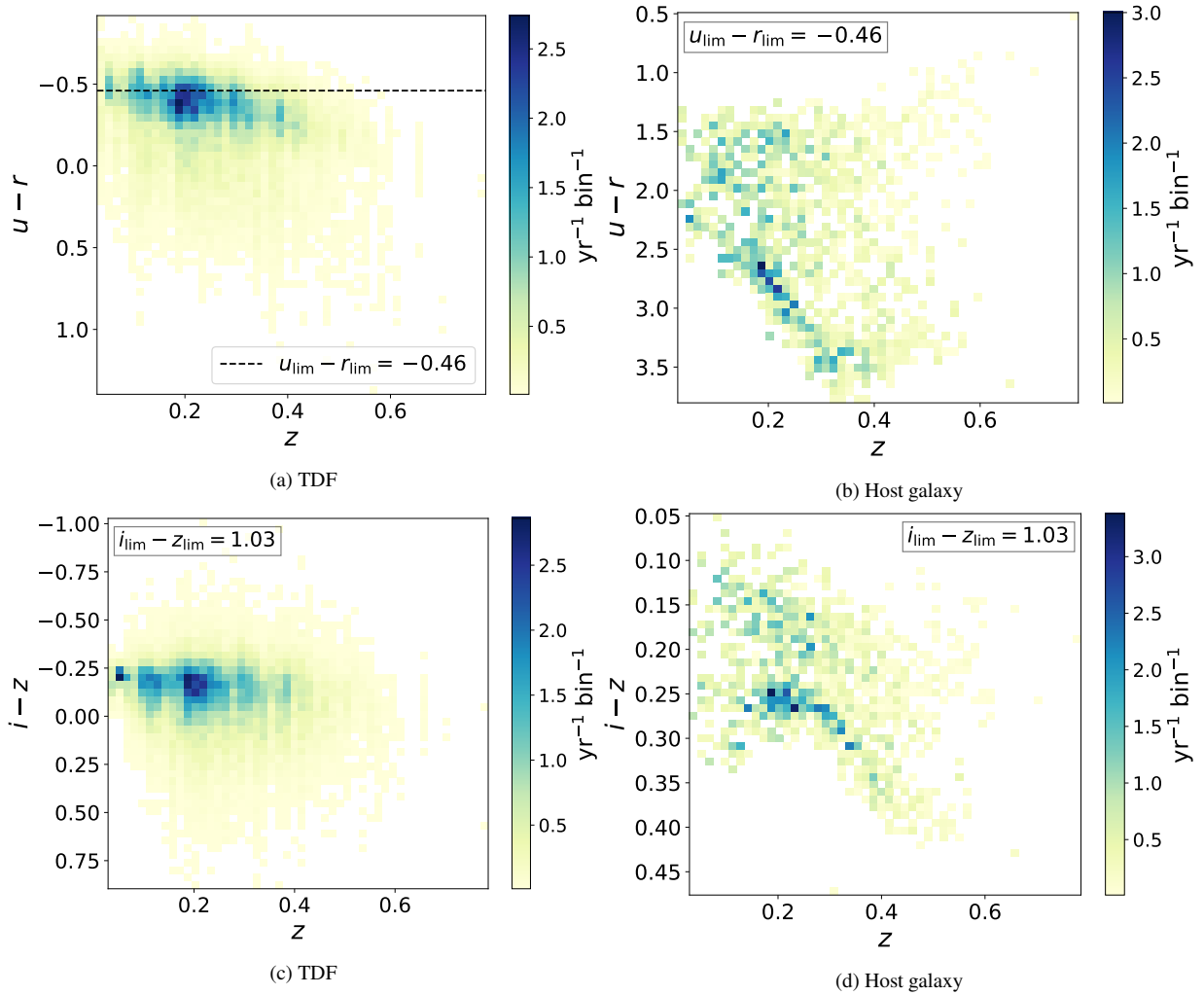


Figure 6. Top panels: the $u - r$ colour of detectable TDFs (left) and host galaxies (right). For most TDFs and almost all host galaxies, the colour is redder than the difference between the limiting magnitude of u and r band, which is $u_{\text{lim}} - r_{\text{lim}} = -0.46$ (dashed horizontal line). As a result, u band cannot significantly increase the detection rate of TDE when both g and r band have been included in the observations. Bottom panels: similar to top panels yet $i - z$ colour has been shown. The difference between the limiting magnitude of i and z band is $i_{\text{lim}} - z_{\text{lim}} = 1.03$, that is redder than the $i - z$ colour of TDFs and host galaxies. Therefore, z band contributes little to the TDE detection.

roughly in agreement with the results of [van Velzen \(2018\)](#), as shown in Figure 10. In the future WFST surveys, we may obtain a better real LF basing on larger TDE samples, which will certainly promote our understanding of the optical emission of TDEs.

4.4.4 Notes on the predicted detection rate

If we choose an observational cadence of 10 days with u , g , r , i filters, WFST can find 29 ± 6 TDEs per year in 440 deg^2 under the sky background level of 22 mag/arcsec^2 . To examine the reliability of the predicted rate, we use the scaling relation from [van Velzen et al. \(2011\)](#), that the rate should obey $\dot{N}_{\text{obs}} \propto f_{\text{sky}} F_{\text{lim}}^{-3/2}$, where f_{sky} and F_{lim} represent the survey fraction of the whole sky and flux limit, respectively. As a reference, ZTF-I survey has discovered 30 TDEs in $15,000 \text{ deg}^2$ sky area in 32 months, indicating a discovery rate of $\sim 12 \text{ yr}^{-1}$ ([Hammerstein et al. 2022](#)). Assuming the flux limit of ZTF and WFST are both determined by r -band limiting magnitude, which is 20.5 mag and 22.8 mag, respectively, WFST should discover ~ 8 TDEs per year in the 440 deg^2 field. This is a factor of ~ 3.5 below our prediction. As ZTF-I TDEs all have follow-up spectroscopic, X-ray

and UV data, it may suggest that some TDEs have been prevented from final identification due to the limited follow-up resources.

We turn to “the top of the iceberg,” the ZTF Bright Transient Survey ([Perley et al. 2020](#)), which covers the same sky area as ZTF. It is spectroscopically complete down to 18.5 mag, and has detected 5 TDEs in 25.5 months. We examine the scaling relation again, and it yields a detection rate of ~ 26 TDEs per year in the 440 deg^2 field. This is now consistent with our prediction.

In addition, the theoretical TDE rate formula we use (Eq. 2) has probably contributed to an overestimate of the TDE detection rate. The reason is that the formula accounts for all TDEs. We use the MOSFiT model to generate light curves for only optically-bright TDEs. Therefore, the TDE rate assigned is precise only when all TDEs are optically-bright. However, a recent X-ray selected sample from eROSITA has unveiled a new class of TDEs, which are X-ray-bright but optically-faint ([Sazonov et al. 2021](#)). Despite this omission, the TDE rate estimated from eROSITA sample is $(1.1 \pm 0.5) \times 10^{-5} \text{ gal}^{-1} \text{ yr}^{-1}$, that is one order of magnitude lower than $\sim 10^{-4} \text{ gal}^{-1} \text{ yr}^{-1}$, as suggested by both optical TDE sample ([van Velzen et al. 2020](#)) and the formula we use (both the results of [Stone & Metzger](#)

Table 3. Results of $10\times 10\times 10$ mock observations: The impact of threshold, cadence and l_2

Threshold k	10	10	5	5	10	10	5	5
Cadence C (d)	10	20	10	20	10	20	10	20
l_2	1	1	1	1	2	2	2	2
<i>ug</i>	11(290)	4(183)	16(428)	11(517)	1(32)	0(23)	2(46)	1(58)
<i>ur</i>	17(460)	5(233)	27(732)	18(833)	1(26)	0(15)	1(39)	1(45)
<i>ui</i>	14(373)	4(172)	23(612)	14(674)	1(21)	0(10)	1(33)	1(38)
<i>gr</i>	28(757)	10(479)	41(1108)	29(1362)	15(400)	6(292)	21(558)	15(715)
<i>gi</i>	17(445)	5(219)	27(713)	17(807)	11(294)	4(168)	17(446)	11(530)
<i>ri</i>	17(466)	5(224)	28(754)	18(846)	17(443)	5(218)	26(705)	17(801)
<i>ugr</i>	29(512)	11(378)	42(747)	30(1054)	15(274)	7(236)	21(381)	16(561)
<i>ugi</i>	19(340)	6(213)	30(528)	20(702)	12(221)	5(162)	18(323)	13(453)
<i>uri</i>	20(358)	6(213)	32(563)	21(743)	18(328)	6(199)	29(511)	19(677)
<i>gri</i>	29(515)	10(369)	42(756)	30(1060)	25(455)	9(334)	37(661)	26(936)
<i>ugri</i>	29(392)	11(286)	43(573)	30(807)	26(346)	10(260)	38(503)	27(714)
<i>ugriz</i>	29(314)	11(229)	43(459)	30(646)	26(277)	10(208)	38(402)	27(571)

Notes:

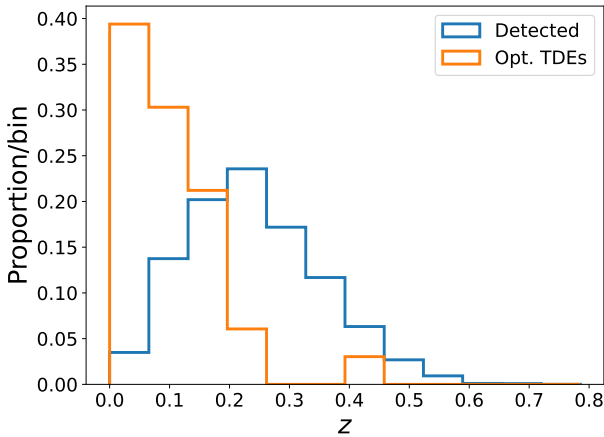
1. Out of parentheses:

Detectable TDEs in 440 deg^2 per year, with threshold, cadence, the minimum number of WFST bands that can detect the host galaxy and band combination altered.

2. In parentheses:

Detectable TDEs in maximum survey area per year, with threshold, cadence, the minimum number of WFST bands that can detect the host galaxy and band combination altered. The maximum survey area are calculated based on the WFST scanning speed (assuming 4-hour useful observing time per night, 10-second readout time), with an upper limit of 2π steradian ($\sim 20,600 \text{ deg}^2$) if the band combination can fully cover the full northern celestial sphere. A detailed version of this table is displayed in appendix (see Table A1).

3. Explanations on key parameters:

Threshold k : The minimum times that the TDF should be detected in a band of WFST.Cadence C : The interval between two closest observations in any band of WFST. l_2 : The minimum number of WFST bands that can detect the host galaxy.**Figure 7.** The histogram of TDE redshift distribution according to our $10\times 10\times 10$ mock observations of the 440 deg^2 sky region. The blue histogram shows the result from the mock detection based on 100-second reference images, while the orange histogram represents the distribution of the 33 optical-selected TDEs reviewed in Table 1 of van Velzen et al. (2020). Compared with real sample, WFST shows great performance in detecting TDEs at higher redshifts, up to $z \sim 0.8$.

(2016) and Section 2.2). Besides, the connections between X-ray and optical emission of TDEs remain unclear, as some TDEs are both detectable in X-ray and optical bands. Actually, among 13 eROSITA TDEs, 4 are detectable in optical surveys, and thus can be categorized into optically-bright TDEs. Therefore, we conclude that the X-ray-

bright and optically-faint population occupy only a small fraction ($<10\%$) of the whole TDE family and thus they will not affect our results significantly.

Given the WFST scanning speed (assuming 4-hour useful observing time per night and 10-second readout time), we can calculate the maximum survey area for this survey strategy. In this way, we estimate that 392 ± 74 TDEs per year can be discovered if the survey program is fully optimized for TDE search. This rate is about an order less than VRO/LSST predictions. For example, Roth et al. (2021) recently gives a very conservative detection rate of $\sim 1,600/\text{yr}$ for VRO/LSST. However, they have abandoned all flares in galaxies with $m_r > 22$, which is far shallower than the depth of VRO. As a result, they have missed most TDEs in dwarf or distant galaxies (see Figure 11) and thus the real detection ability of VRO could be likely even more powerful. In any case, in the upcoming VRO and WFST era, the anticipated TDE candidates will be massive and challenge the follow-up resources, such as spectroscopic observations.

5 CONCLUSIONS

The 2.5-metre WFST is going to start a wide-field, fast and deep time-domain survey soon. In order to evaluate its survey ability, we have carried out mock observations of TDEs, and explored the influence of various factors. Our main results are summarized as below.

- We define a discovery of TDE as ≥ 10 epochal detections in at least two bands. If we choose an observational cadence of 10 days with u, g, r, i filters, WFST can find 29 ± 6 TDEs per year in 440 deg^2 under the sky background level of 22 mag/arcsec^2 . Given the

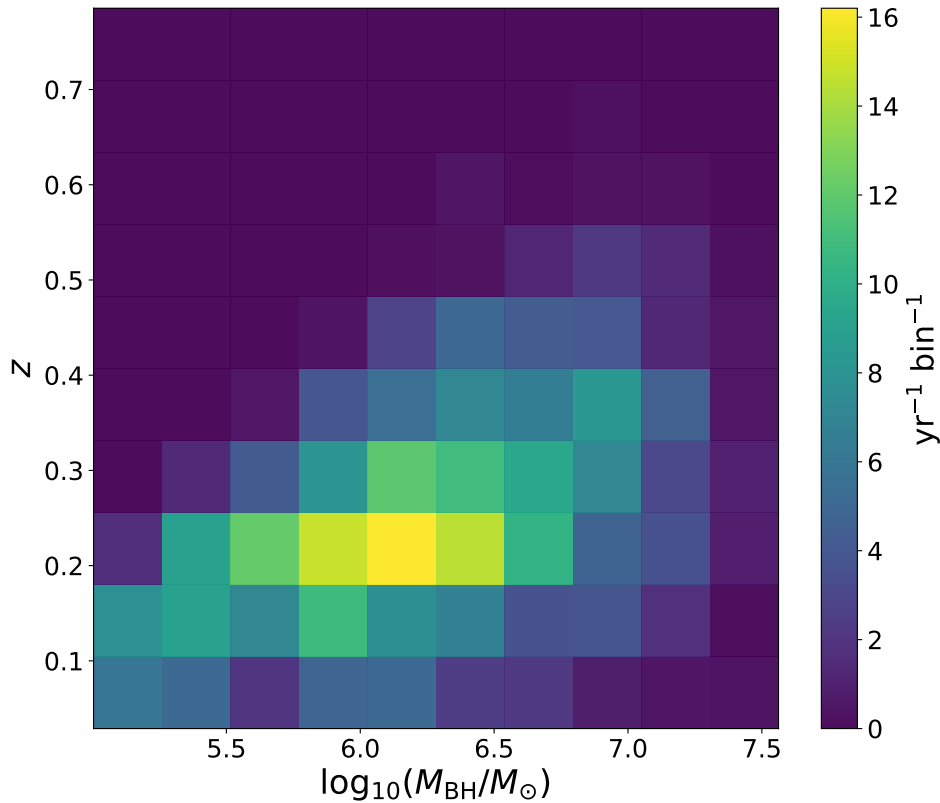


Figure 8. The z and M_{BH} distribution of detected TDEs. To minimize the stochastic errors, we show the average count of detectable TDEs in the $10 \times 10 \times 10$ mock observations, that is equivalent to a one-year observation in sky area of 440 deg^2 . TDEs occurring in smaller BHs, which usually resides in more dwarf galaxies, can be only detected at lower redshift.

WFST scanning speed (assuming 4-hour useful observing time per night and 10-second readout time), we can calculate the maximum survey area for this survey strategy. In this way, we estimate that 392 ± 74 TDEs per year can be discovered if the survey program is fully optimized for TDE search.

- g and r bands are most useful for the TDE detection; u band cannot significantly increase the detection rate when both g and r bands are already used. However, it should still be important since it provides the radiation information closest to the SED peak of TDEs, which is crucial for distinguishing TDEs from other transients (e.g., by its blackbody temperature).

- The sky background affects the results only when $I_{\text{sky}} < 20 \text{ mag/arcsec}^2$. The readout noise slightly prevents high-redshift TDEs from detection.

- Our mock observation yields TDEs up to $z \sim 0.8$, with the largest number density at $z \sim 0.2 - 0.3$. The g -band absolute magnitude (M_g) distribution and the luminosity function roughly agree with the real optical TDE sample.

ACKNOWLEDGEMENTS

We thank the expert referee for his/her very constructive comments and suggestions. We thank Tingui Wang, Lulu Fan, Zhengyan Liu, Zesen Lin and Zhixiong Liang for very useful discussions and suggestions. This work is supported by the Strategic Priority Research Program of Chinese Academy of Sciences (No. XDB 41000000), the National Key R&D Program of China (2017YFA0402600), the NSFC grant (Nos. 11833007, 11973038, 12073025), the Chinese

Space Station Telescope (CSST) Project and the Fundamental Research Funds for the Central Universities.

DATA AVAILABILITY

The data underlying this article will be shared on reasonable request to the corresponding author.

REFERENCES

- Arcavi, I., Gal-Yam, A., Sullivan, M., et al. 2014, *ApJ*, 793, 38. doi:10.1088/0004-637X/793/1/38
- Bade, N., Komossa, S., & Dahlem, M. 1996, *A&A*, 309, L35
- Bellm, E. C., Kulkarni, S. R., Graham, M. J., et al. 2019, *PASP*, 131, 018002. doi:10.1088/1538-3873/aacbbe
- Beloborodov, A. M., Illarionov, A. F., Ivanov, P. B., et al. 1992, *MNRAS*, 259, 209. doi:10.1093/mnras/259.2.209
- Bloom, J. S., Giannios, D., Metzger, B. D., et al. 2011, *Science*, 333, 203. doi:10.1126/science.1207150
- Bricman, K. & Gomboc, A. 2020, *ApJ*, 890, 73. doi:10.3847/1538-4357/ab6989
- Calzetti, D., Armus, L., Bohlin, R. C., et al. 2000, *ApJ*, 533, 682. doi:10.1086/308692
- Cinzano, P. 2005, *Intern. Rep. ISTIL*, 9, 1–13
- Dai, L., McKinney, J. C., Roth, N., et al. 2018, *ApJ*, 859, L20. doi:10.3847/2041-8213/aab429
- Deng, L., Yang, F., Chen, X., et al. 2021, *Nature*, 596, 353. doi:10.1038/s41586-021-03711-z

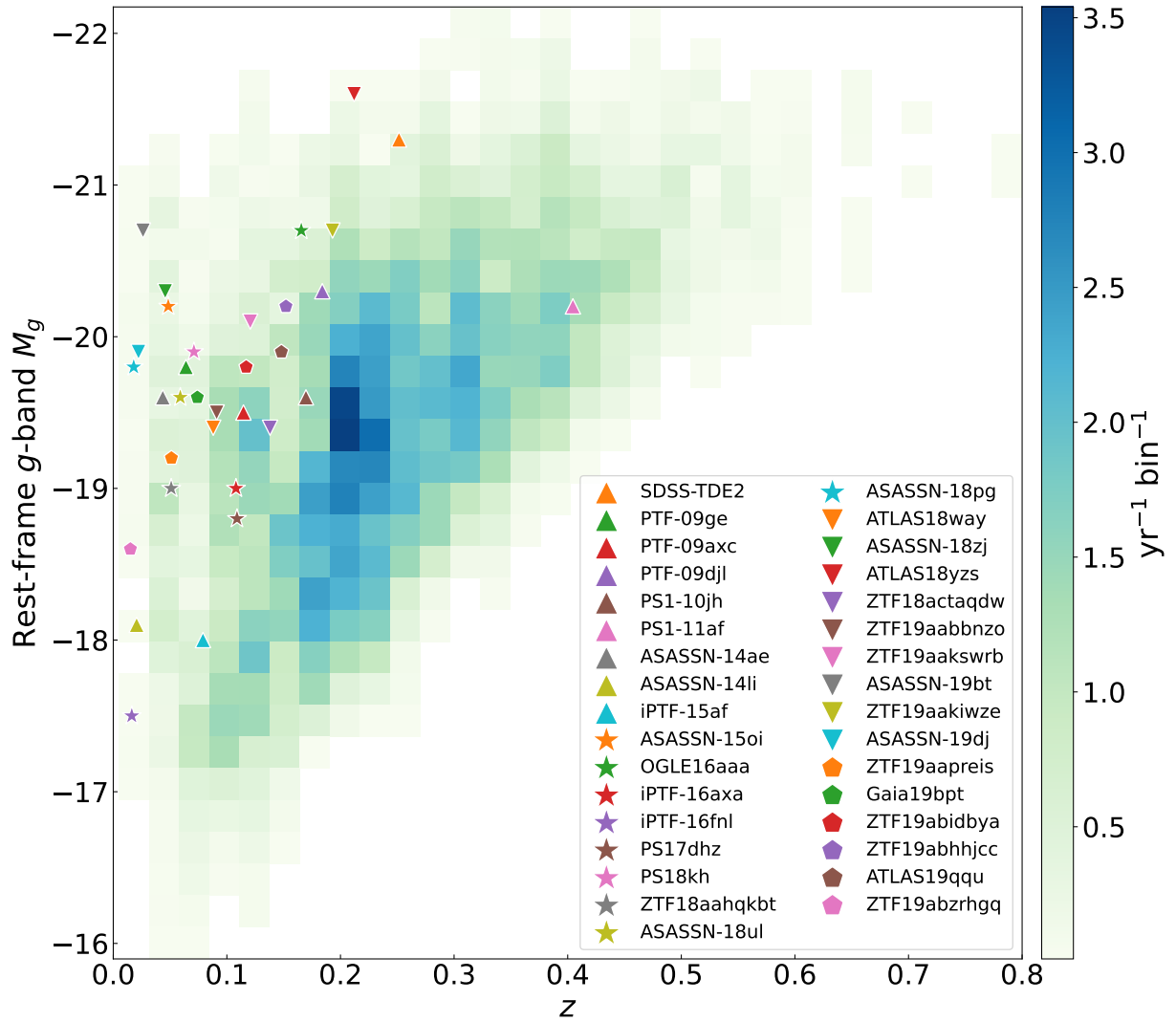


Figure 9. The peak absolute g-band magnitude (M_g) as function of redshift for TDEs detected in our mock observations. To minimize the stochastic errors, we show the average count of detectable TDEs in the $10 \times 10 \times 10$ mock observations, that is equivalent to a one-year observation in sky area of 440 deg^2 . We have also overplotted the 33 optical TDEs summarized in Table 1 of van Velzen et al. (2020) for comparison. The distribution of mocked TDE sample is generally in accordance with real optical TDEs, especially in luminosity, yet it has extended to higher redshift (see also Figure 7).

Donley, J. L., Brandt, W. N., Eracleous, M., et al. 2002, *AJ*, 124, 1308. doi:10.1086/342280

Esquej, P., Saxton, R. D., Freyberg, M. J., et al. 2007, *A&A*, 462, L49. doi:10.1051/0004-6361/20066072

Evans, C. R. & Kochanek, C. S. 1989, *ApJ*, 346, L13. doi:10.1086/185567

Garn, T. & Best, P. N. 2010, *MNRAS*, 409, 421. doi:10.1111/j.1365-2966.2010.17321.x

Gezari, S., Martin, D. C., Milliard, B., et al. 2006, *ApJ*, 653, L25. doi:10.1086/509918

Gezari, S., Basa, S., Martin, D. C., et al. 2008, *ApJ*, 676, 944. doi:10.1086/529008

Gezari, S., Chornock, R., Rest, A., et al. 2012, *Nature*, 485, 217. doi:10.1038/nature10990

Gezari, S. 2021, *ARA&A*, 59. doi:10.1146/annurev-astro-111720-030029

González Delgado, R. M., García-Benito, R., Pérez, E., et al. 2015, *A&A*, 581, A103. doi:10.1051/0004-6361/201525938

Guillochon, J. & Ramirez-Ruiz, E. 2013, *ApJ*, 767, 25. doi:10.1088/0004-637X/767/1/25

Guillochon, J., Nicholl, M., Villar, V. A., et al. 2018, *ApJS*, 236, 6. doi:10.3847/1538-4365/aab761

Hammerstein, E., van Velzen, S., Gezari, S., et al. 2022, *arXiv:2203.01461*

Hills, J. G. 1975, *Nature*, 254, 295. doi:10.1038/254295a0

Holoien, T. W.-S., Kochanek, C. S., Prieto, J. L., et al. 2016, *MNRAS*, 455, 2918. doi:10.1093/mnras/stv2486

Ivezić, Ž., Kahn, S. M., Tyson, J. A., et al. 2019, *ApJ*, 873, 111. doi:10.3847/1538-4357/ab042c

Jiang, N., Dou, L., Wang, T., et al. 2016, *ApJ*, 828, L14. doi:10.3847/2041-8205/828/1/L14

Jiang, N., Wang, T., Hu, X., et al. 2021, *ApJ*, 911, 31. doi:10.3847/1538-4357/abc772

Jones, D. O., Scolnic, D. M., & Rodney, S. A. 2015, *Astrophysics Source Code Library*. ascl:1501.010

Komossa, S. & Bade, N. 1999, *A&A*, 343, 775

Korytov, D., Hearin, A., Kovacs, E., et al. 2019, *ApJS*, 245, 26. doi:10.3847/1538-4365/ab510c

Leloudas, G., Fraser, M., Stone, N. C., et al. 2016, *Nature Astronomy*, 1, 0002. doi:10.1038/s41550-016-0002

Lin, D., Strader, J., Carrasco, E. R., et al. 2018, *Nature Astronomy*, 2, 656. doi:10.1038/s41550-018-0493-1

Liu, F. K., Li, S., & Komossa, S. 2014, *ApJ*, 786, 103. doi:10.1088/0004-637X/786/2/103

Liu, F. K., Cao, C. Y., Abramowicz, M. A., et al. 2021, *ApJ*, 908, 179.

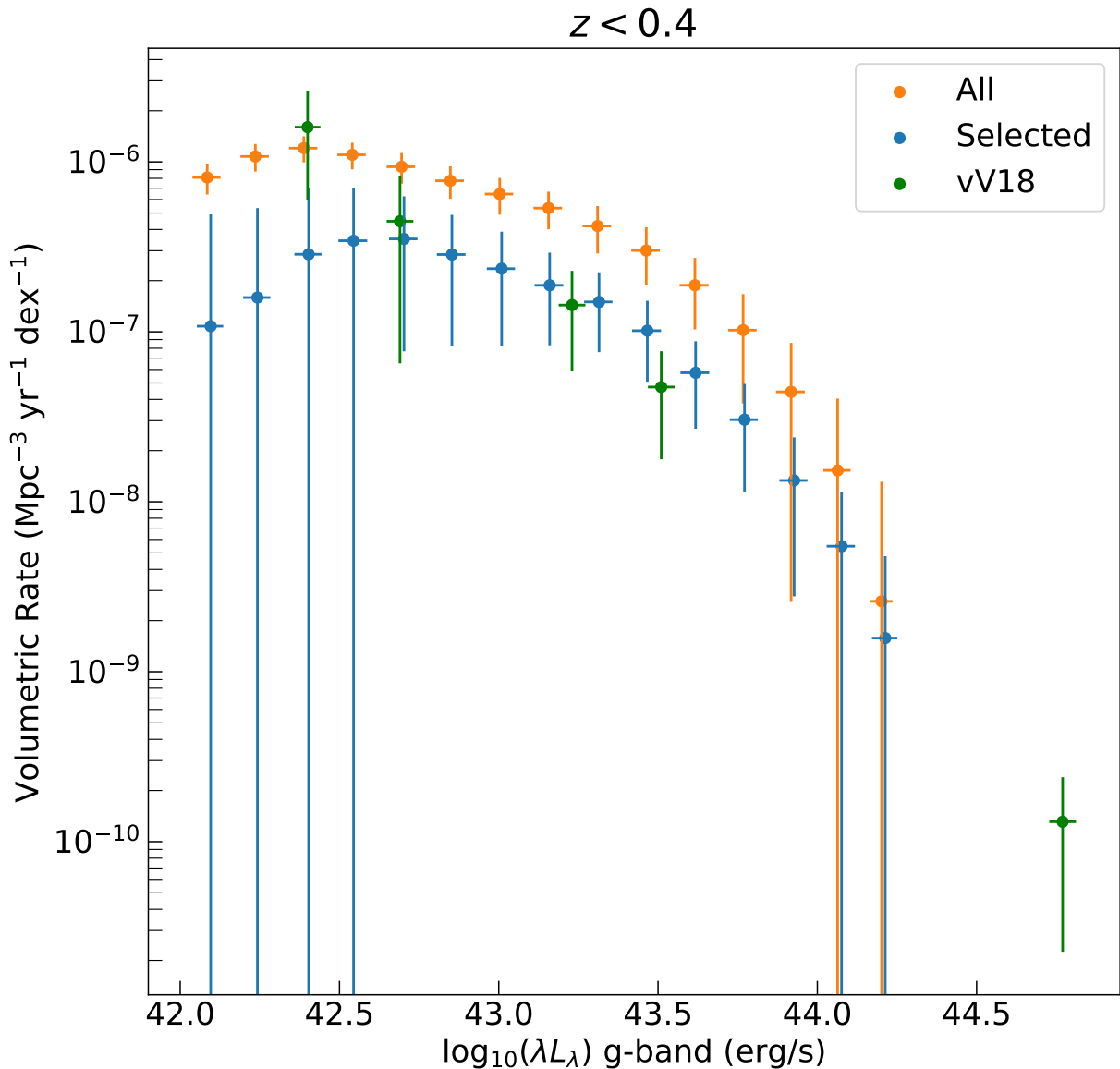


Figure 10. The luminosity function of detected TDFs (blue) and all TDFs (orange) within $z = 0.4$ for 1000 mock observations. For detected mock TDFs, we perform the volumetric correction, i.e., " $1/V_{\max}$ " method following van Velzen (2018). The luminosity function of van Velzen (2018) is also overplotted in green for comparison.

- doi:10.3847/1538-4357/abd2b6
 Lu, W. & Bonnerot, C. 2020, MNRAS, 492, 686. doi:10.1093/mnras/stz3405
 Lou, Z., Liang, M., Yao, D., et al. 2016, Proc. SPIE, 10154, 101542A. doi:10.1117/12.2248371
 LSST Science Collaboration, Abell, P. A., Allison, J., et al. 2009, arXiv:0912.0201
 Mageshwaran, T. & Mangalam, A. 2015, ApJ, 814, 141. doi:10.1088/0004-637X/814/2/141
 Maguire, K., Eracleous, M., Jonker, P. G., et al. 2020, Space Sci. Rev., 216, 39. doi:10.1007/s11214-020-00661-2
 Maksym, W. P., Ulmer, M. P., & Eracleous, M. 2010, ApJ, 722, 1035. doi:10.1088/0004-637X/722/2/1035
 Mockler, B., Guillochon, J., & Ramirez-Ruiz, E. 2019, ApJ, 872, 151. doi:10.3847/1538-4357/ab010f
 O'Donnell, J. E. 1994, ApJ, 422, 158. doi:10.1086/173713
 Pasham, D. R., Remillard, R. A., Fragile, P. C., et al. 2019, Science, 363, 531. doi:10.1126/science.aar7480
 Perley, D. A., Fremling, C., Sollerman, J., et al. 2020, ApJ, 904, 35. doi:10.3847/1538-4357/abbd98
 Phinney, E. S. 1989, The Center of the Galaxy, IAU Symp., 136, 543
 Piran, T., Svirski, G., Krolik, J., et al. 2015, ApJ, 806, 164. doi:10.1088/0004-637X/806/2/164
 Rees, M. J. 1988, Nature, 333, 523. doi:10.1038/333523a0
 Roth, N., Kasen, D., Guillochon, J., et al. 2016, ApJ, 827, 3. doi:10.3847/0004-637X/827/1/3
 Roth, N., Rossi, E. M., Krolik, J., et al. 2020, Space Sci. Rev., 216, 114. doi:10.1007/s11214-020-00735-1
 Roth, N., van Velzen, S., Cenko, S. B., et al. 2021, ApJ, 910, 93. doi:10.3847/1538-4357/abdf50
 Rowe, B. T. P., Jarvis, M., Mandelbaum, R., et al. 2015, Astronomy and Computing, 10, 121. doi:10.1016/j.ascom.2015.02.002
 Saxton, R., Komossa, S., Auchettl, K., et al. 2020, Space Sci. Rev., 216, 85. doi:10.1007/s11214-020-00708-4
 Sazonov, S., Gilfanov, M., Medvedev, P., et al. 2021, MNRAS, 508, 3820. doi:10.1093/mnras/stab2843
 Shi, D. D., Zheng, X. Z., Zhao, H. B., et al. 2018, Acta Astronomica Sinica,

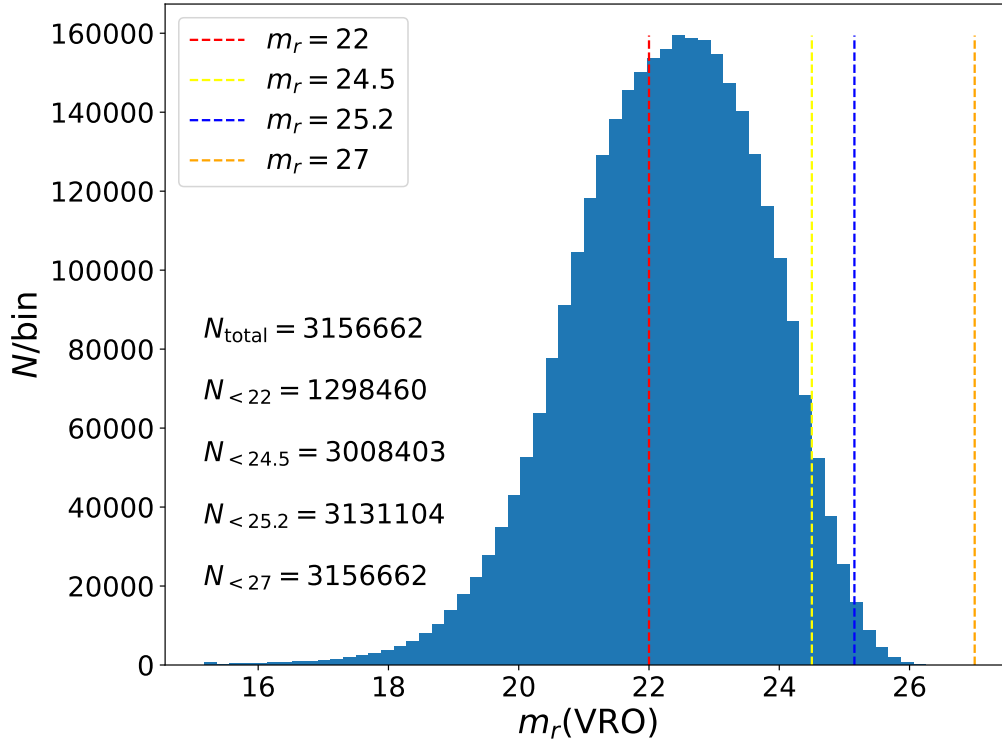


Figure 11. The m_r (VRO) distribution for galaxies with $10^5 M_\odot \leq M_{\text{BH}} \leq 9 \times 10^7 M_\odot$ and $z < 0.45$ in the CosmoDC2 catalogue, that matches the black hole mass and redshift ranges available for the TDE hosts, as presented in the Figure 24 of Roth et al. (2021). The flux-limited catalogue they used excludes any flares coming from galaxies with $m_r > 22$. Given the VRO depth ($m_r = 24.5$ and 25.2 under 30-second and 100-second exposures, respectively, and $m_r \approx 27$ after the 10-year survey) and $z < 0.45$, the number of galaxies will be ≈ 1.5 times more by choosing the magnitude cut of $m_r = 24.5$ instead of $m_r = 22$. Moreover, the redshift limit $z_{\text{lim}} = 0.45$ can actually be higher given a greater limiting magnitude, resulting in a more serious omission of possible TDE hosts (≈ 4.5 times if $z_{\text{lim}} = 0.8$). And if the host galaxy detection is performed on stacked images, the number of detectable TDEs will be even larger. Therefore, the predicted VRO detection rate given in Roth et al. (2021) is severely underestimated because they have put a very shallow magnitude cut for host galaxies, although the cut is reasonable for ZTF ($\approx 30\%$ for $z_{\text{lim}} = 0.25$).

59, 22

- Shu, X., Zhang, W., Li, S., et al. 2020, Nature Communications, 11, 5876. doi:10.1038/s41467-020-19675-z
- Stone, N. C. & Metzger, B. D. 2016, MNRAS, 455, 859. doi:10.1093/mnras/stv2281
- Strubbe, L. E. & Quataert, E. 2009, MNRAS, 400, 2070. doi:10.1111/j.1365-2966.2009.15599.x
- Thorp, S., Chadwick, E., & Sesana, A. 2019, MNRAS, 488, 4042. doi:10.1093/mnras/stz1970
- van Velzen, S., Farrar, G. R., Gezari, S., et al. 2011, ApJ, 741, 73. doi:10.1088/0004-637X/741/2/73
- van Velzen, S. & Farrar, G. R. 2014, ApJ, 792, 53. doi:10.1088/0004-637X/792/1/53
- van Velzen, S., Mendez, A. J., Krolik, J. H., et al. 2016, ApJ, 829, 19. doi:10.3847/0004-637X/829/1/19
- van Velzen, S. 2018, ApJ, 852, 72. doi:10.3847/1538-4357/aa998e
- van Velzen, S., Holoien, T. W.-S., Onori, F., et al. 2020, Space Sci. Rev., 216, 124. doi:10.1007/s11214-020-00753-z
- van Velzen, S., Gezari, S., Hammerstein, E., et al. 2021, ApJ, 908, 4. doi:10.3847/1538-4357/abc258

APPENDIX A: DETAILED VERSION OF TABLE 3

This paper has been typeset from a $\text{\TeX}/\text{\LaTeX}$ file prepared by the author.

Table A1. Full results of 10×10×10 mock observations

Threshold k	10	10	5	5
Cadence C (d)	10	20	10	20
l_2	1	1	1	1
<i>ug</i>	10.8±3.3(289.8±89.5)	3.9±2.1(182.9±99.4)	16.0±4.0(427.8±106.4)	11.0±3.3(517.3±156.7)
<i>ur</i>	17.2±4.3(459.9±115.5)	5.0±2.4(232.7±112.7)	27.3±5.5(732.0±148.5)	17.8±4.4(832.7±205.5)
<i>ui</i>	13.9±3.9(373.2±105.7)	3.7±2.1(172.0±96.5)	22.8±5.0(611.6±134.7)	14.4±3.9(673.9±183.6)
<i>gr</i>	28.3±5.4(757.1±145.4)	10.2±3.4(479.3±159.7)	41.3±6.3(1107.9±168.9)	29.1±5.5(1362.5±256.5)
<i>gi</i>	16.6±4.2(445.3±111.5)	4.7±2.2(219.1±104.6)	26.6±5.1(712.8±136.2)	17.2±4.1(806.6±194.3)
Used Bands <i>ri</i>	17.4±4.0(466.4±108.3)	4.8±2.3(223.7±107.0)	28.1±5.1(753.9±135.6)	18.1±4.0(846.2±188.0)
<i>ugr</i>	28.7±5.4(512.2±97.3)	10.6±3.5(378.1±126.0)	41.8±6.3(747.3±113.4)	29.5±5.5(1054.1±196.4)
<i>ugi</i>	19.0±4.6(339.5±81.4)	6.0±2.6(213.4±92.1)	29.5±5.4(527.6±97.0)	19.6±4.6(702.0±164.7)
<i>uri</i>	20.0±4.5(358.0±80.2)	6.0±2.5(212.6±91.0)	31.5±5.6(563.3±99.9)	20.8±4.6(743.4±162.7)
<i>gri</i>	28.8±5.5(515.2±97.8)	10.3±3.4(368.8±122.1)	42.3±6.2(755.5±111.2)	29.7±5.5(1060.5±196.1)
<i>ugri</i>	29.3±5.5(392.0±73.5)	10.7±3.5(286.2±94.8)	42.8±6.3(573.2±83.9)	30.1±5.5(807.1±147.6)
<i>ugriz</i>	29.3±5.5(313.6±58.8)	10.7±3.5(229.0±75.8)	42.8±6.3(458.6±67.1)	30.1±5.5(645.7±118.1)

Threshold k	10	10	5	5
Cadence C (d)	10	20	10	20
l_2	2	2	2	2
<i>ug</i>	1.2±1.1(32.4±28.4)	0.5±0.6(22.9±29.3)	1.7±1.3(46.1±34.7)	1.2±1.1(57.9±49.9)
<i>ur</i>	1.0±0.9(25.5±25.2)	0.3±0.5(15.1±24.7)	1.4±1.2(38.7±31.7)	1.0±0.9(45.4±43.7)
<i>ui</i>	0.8±0.8(20.7±22.4)	0.2±0.5(10.1±21.2)	1.2±1.1(32.6±28.9)	0.8±0.8(37.5±39.5)
<i>gr</i>	14.9±4.1(399.9±108.6)	6.2±2.7(292.3±125.9)	20.8±4.7(557.9±124.7)	15.3±4.1(715.3±192.9)
<i>gi</i>	11.0±3.3(294.5±87.4)	3.6±2.0(168.5±91.5)	16.6±4.0(445.6±106.1)	11.3±3.3(529.6±155.2)
Used Bands <i>ri</i>	16.5±4.1(443.1±111.0)	4.6±2.2(217.8±104.2)	26.3±5.1(704.9±135.8)	17.1±4.1(801.0±193.8)
<i>ugr</i>	15.3±4.1(274.0±73.1)	6.6±2.8(235.5±99.9)	21.3±4.6(380.6±82.9)	15.7±4.1(560.8±147.8)
<i>ugi</i>	12.4±3.6(221.3±63.9)	4.5±2.2(162.4±79.1)	18.1±4.2(323.0±74.4)	12.7±3.6(453.3±128.0)
<i>uri</i>	18.4±4.5(328.4±80.3)	5.6±2.4(199.1±87.4)	28.6±5.4(510.7±96.7)	19.0±4.6(677.4±163.2)
<i>gri</i>	25.4±5.2(454.6±92.5)	9.4±3.4(334.4±120.7)	37.0±5.7(661.4±101.5)	26.2±5.2(935.6±185.8)
<i>ugri</i>	25.9±5.2(346.5±70.0)	9.7±3.5(260.4±93.8)	37.5±5.7(502.6±76.6)	26.6±5.2(713.5±140.6)
<i>ugriz</i>	25.9±5.2(277.2±56.0)	9.7±3.5(208.3±75.0)	37.5±5.7(402.1±61.3)	26.6±5.2(570.8±112.5)

Notes:

1. Out of parentheses:

Detectable TDEs in 440 deg² per year, with threshold, cadence, the minimum number of WFST bands that can detect the host galaxy and band combination altered.

2. In parentheses:

Detectable TDEs in maximum survey area per year, with threshold, cadence, the minimum number of WFST bands that can detect the host galaxy and band combination altered. The maximum survey area are calculated based on the WFST scanning speed (assuming 4-hour useful observing time per night, 10-second readout time), with an upper limit of 2π steradian ($\sim 20,600$ deg²) if the band combination can fully cover the full northern celestial sphere.

3. Explanations on key parameters:

Threshold k : The minimum times that the TDF should be detected in a band of WFST.Cadence C : The interval between two closest observations in any band of WFST. l_2 : The minimum number of WFST bands that can detect the host galaxy.